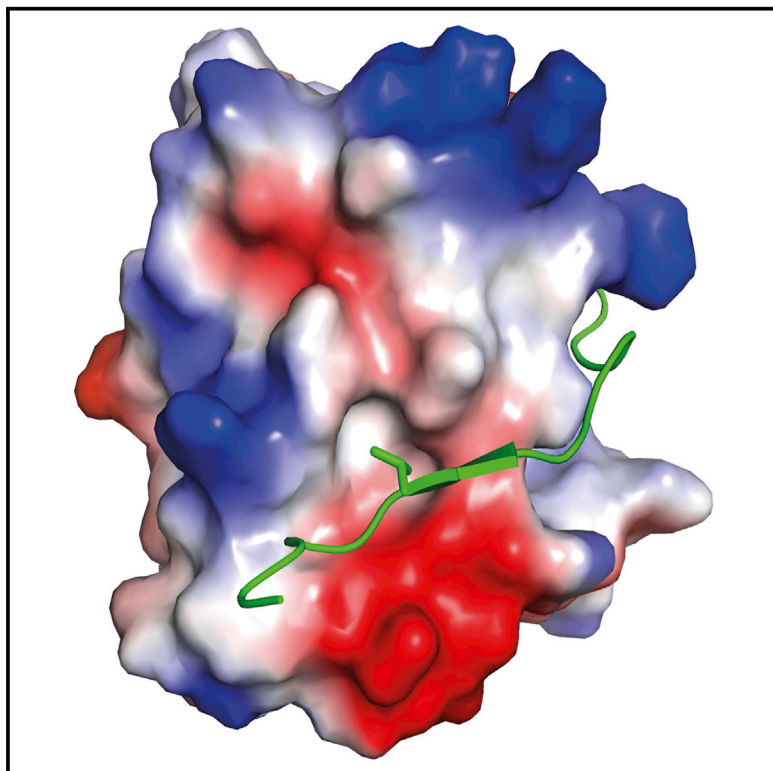


Structure

VirB7 and VirB9 Interactions Are Required for the Assembly and Antibacterial Activity of a Type IV Secretion System

Graphical Abstract



Authors

Luciana Coutinho Oliveira,
Diorge Paulo Souza,
Gabriel Umaji Oka, ..., Rolf Boelens,
Chuck Shaker Farah,
Roberto Kopke Salinas

Correspondence

diorge@iq.usp.br (D.P.S.),
chsfarah@iq.usp.br (C.S.F.),
roberto@iq.usp.br (R.K.S.)

In Brief

Oliveira et al. show that tight binding of VirB7 to VirB9 is essential for assembly of the antibacterial type IV secretion system (T4SS) in the citrus pathogen *Xanthomonas citri*, whereas removal of the non-canonical VirB7 C-terminal domain, or impairment of VirB7 self-association, does not perturb assembly but abolishes T4SS activity.

Highlights

- Binding to VirB7^{NT} stabilizes VirB9^{CT}
- The structural basis of the recognition between VirB7 and VirB9 is revealed
- Disruption of VirB7-VirB9 interaction affects T4SS assembly and killing activity
- Interactions between VirB7 subunits are essential for a functional T4SS

Accession Numbers

AAM37471.1
AAM37469.1
2N01



VirB7 and VirB9 Interactions Are Required for the Assembly and Antibacterial Activity of a Type IV Secretion System

Luciana Coutinho Oliveira,^{1,4} Diorge Paulo Souza,^{1,*} Gabriel Umaji Oka,¹ Filipe da Silva Lima,¹ Ronaldo Junio Oliveira,² Denize Cristina Favaro,^{1,5} Hans Wienk,³ Rolf Boelens,³ Chuck Shaker Farah,^{1,*} and Roberto Kopke Salinas^{1,6,*}

¹Departamento de Bioquímica, Instituto de Química, Universidade de São Paulo, São Paulo, São Paulo 05508-000, Brazil

²Departamento de Física, Instituto de Ciências Exatas e Naturais, Universidade Federal do Triângulo Mineiro, Uberaba, Minas Gerais 38064-200, Brazil

³NMR Spectroscopy, Bijvoet Center for Biomolecular Research, Utrecht University, Utrecht 3584-CH, the Netherlands

⁴Present Address: Department of Pathology and Cell Biology, Institute for Research in Immunology and Cancer (IRIC), University of Montreal, Montreal, QC H3T 1J4, Canada

⁵Present Address: Departamento de Química, Instituto de Ciências Exatas, Universidade Federal de Minas Gerais, Belo Horizonte, Minas Gerais 31270-901, Brazil

⁶Lead Contact

*Correspondence: diorge@iq.usp.br (D.P.S.), chsfarah@iq.usp.br (C.S.F.), roberto@iq.usp.br (R.K.S.)

<http://dx.doi.org/10.1016/j.str.2016.07.015>

SUMMARY

The type IV secretion system (T4SS) from the phytopathogen *Xanthomonas citri* (*Xac*) is a bactericidal nanomachine. The T4SS core complex is a ring composed of multiple copies of VirB7-VirB9-VirB10 subunits. *Xac*-VirB7 contains a disordered N-terminal tail (VirB7^{NT}) that recognizes VirB9, and a C-terminal domain (VirB7^{CT}) involved in VirB7 self-association. Here, we show that VirB7^{NT} forms a short β strand upon binding to VirB9 and stabilizes it. A tight interaction between them is essential for T4SS assembly and antibacterial activity. Abolishing VirB7 self-association or deletion of the VirB7 C-terminal domain impairs this antibacterial activity without disturbing T4SS assembly. These findings reveal protein interactions within the core complex that are critical for the stability and activity of a T4SS.

INTRODUCTION

Bacteria use specialized systems in order to secrete substrates to the environment or deliver them to other cells. Translocation is mediated by membrane-spanning supramolecular protein assemblies called secretion systems (Costa et al., 2015). The type IV secretion system (T4SS) has been shown to carry out a variety of functions in different bacterial species, including translocation of virulence factors to eukaryotic hosts, plasmidial conjugation (exchange of DNA between bacteria), and uptake or release of DNA (Alvarez-Martinez and Christie, 2009; Zechner et al., 2012). *Xanthomonas citri* pv. *citri* (*Xac*) is a Gram-negative bacterium that infects citrus plants causing citrus canker, a disease that has a large agricultural and economic impact worldwide (Brunings and Gabriel, 2003; Büttner and Bonas, 2010;

Das, 2003; Mansfield et al., 2012; Ryan et al., 2011). *Xac*'s chromosomally encoded T4SS is not directly involved in infection (Souza et al., 2011). Rather, it is responsible for the secretion of toxins that kill other gram-negative bacteria (Souza et al., 2015).

A significant amount of structural information has been obtained in recent years on conjugative T4SSs from a combination of X-ray diffraction, single-particle electron microscopy, and solution and solid-state nuclear magnetic resonance (NMR) spectroscopy (Bayliss et al., 2007; Chandran et al., 2009; Fronzes et al., 2009; Kaplan et al., 2015; Low et al., 2014; Rivera-Calzada et al., 2013). The prototypical T4SS is a nanomachine made from a dozen different proteins, VirB1-VirB11 and VirD4, organized in at least two large complex assemblies (Trokter et al., 2014). The first assembly is the core complex, a toroidal structure formed by 14 repetitions of the VirB7-VirB9-VirB10 heterotrimer. The core complex is subdivided in two layers (Chandran et al., 2009; Fronzes et al., 2009; Rivera-Calzada et al., 2013). The outer layer corresponds to VirB7, a lipoprotein that is anchored in the outer membrane, and the C-terminal domains of VirB9 and VirB10. The inner layer consists of the N-terminal domains of VirB9 and part of the N-terminal domain of VirB10. The second large complex assembly is called the inner membrane complex (Low et al., 2014). It consists of the remaining part of the N-terminal domain of VirB10 and a set of other inner membrane-associated proteins including VirB3, VirB4, VirB5, VirB6, and VirB8 (Low et al., 2014).

While a fair amount of structural information is now available for the conjugative T4SSs (Ilangoan et al., 2015), the only piece of structural information that has so far been obtained for a bactericidal T4SS is the three-dimensional structure of *Xac*-VirB7 (Souza et al., 2011). Differently from the canonical VirB7 proteins, *Xac*-VirB7 consists of a flexible N-terminal tail followed by a globular C-terminal domain, the VirB7^{CT} N0 domain, which is absent in the majority of the VirB7 proteins, although it is found in DotD from the type IVB secretion system from *Legionella pneumophila* (Nakano et al., 2010). Previously, we showed that

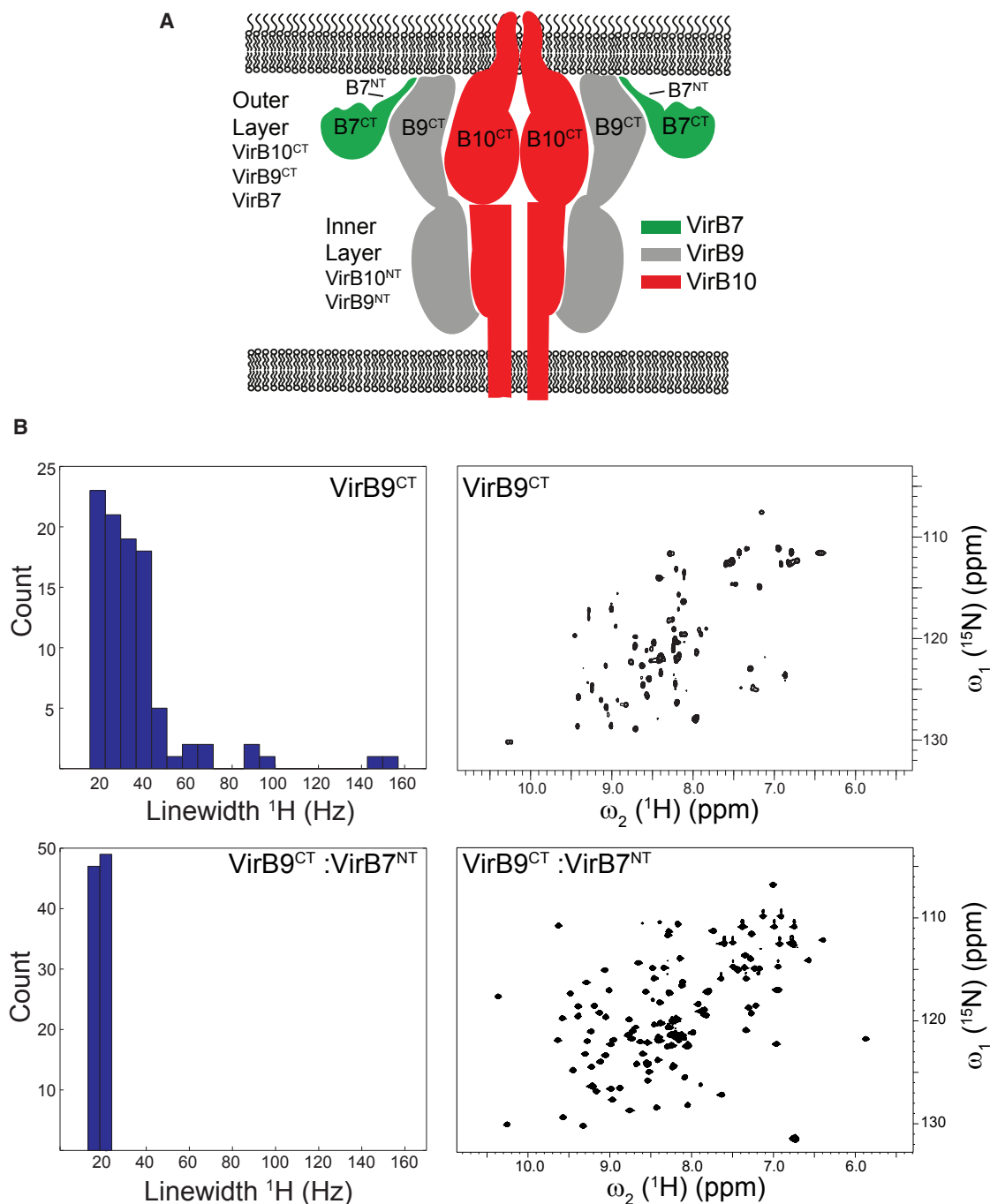


Figure 1. Binding to VirB7^{NT} Stabilizes VirB9^{CT}

(A) Schematic diagram of the core complex of *Xanthomonas citri*'s T4SS.

(B) ¹H-¹⁵N HSQC spectra of unbound VirB9^{CT} and VirB9^{CT} in complex with VirB7^{NT} (right) and distributions of the ¹H-¹⁵N HSQC cross-peaks line widths (left). See also Figure S1.

the N-terminal tail of VirB7 (residues 24–51) is disordered in solution but that the first half (residues 27–41) forms a tight and specific complex with the C-terminal domain of VirB9 (Souza et al., 2011). VirB7^{CT} does not interact with VirB9 but participates in VirB7-VirB7 interactions with the second half of the VirB7 tail (residues 42–49). We have proposed that these VirB7-VirB7

interactions could specifically orient the VirB7^{CT} NO domains around the perimeter of the *Xanthomonas* T4SS core complex (Souza et al., 2011) (Figure 1A). Since the unique *Xanthomonas* VirB7 subunit is a distinguishing feature of Xanthomonadaceae T4SSs (Alegria et al., 2005), we sought to understand the details of its interactions with the other components of the core complex

Table 1. Dissociation Constants, K_d , and Binding Free Energies, ΔG , for the Interactions between VirB7^{NT} Peptide Variants, or the Full-Length VirB7, and VirB9^{CT}

| VirB7 Construct ^a | K_d (μ M) | $-\Delta G$ (kcal/mol) |
|------------------------------|---------------------------|---------------------------|
| Full-length | 1.3 \pm 0.1 | 8.0 |
| Wild-type | 1.0 \pm 0.1 | 8.5 |
| Wild-type | \sim 3.7 ^b | \sim 7.7 ^b |
| D29A | 4.1 \pm 0.3 | 7.6 |
| F30A ^c | 6.6 \pm 1.3 | 6.9 |
| W34A | ND ^d | ND ^d |
| V37G | \sim 825 ^{b,d} | \sim 4.4 ^{b,d} |
| V37A | 9.9 \pm 0.9 | 7.1 |
| V37F | 2.5 \pm 0.1 | 7.9 |
| N38A | 6.1 \pm 0.6 | 7.4 |

All measurements were performed by ITC at 37°C unless otherwise stated. ND, not detected.

^aAll experiments were performed with variants of the peptide VirB7^{NT}, with the exception of the experiment carried out with the full-length VirB7.

^bThe dissociation constant was estimated from the analysis of NMR titration data.

^cThe ITC measurements for the mutant F30A were performed at 20°C.

^dITC signals were not detected in the titration experiments.

and the importance of these interactions for the stability and function of this specialized T4SS. Here we used high-resolution NMR spectroscopy in order to solve the three-dimensional structure of the complex between the N-terminal tail of VirB7 (VirB7^{NT}) and VirB9^{CT}, the C-terminal domain of VirB9. We employed interbacterial competition assays to investigate the contribution of specific VirB7 intermolecular contacts for the stability and function of the T4SS system in vivo. We found that a tight interaction between VirB7 and VirB9 is essential for the in vivo assembly of the T4SS, while interactions between VirB7 subunits are not required for assembly, but are necessary for a functional T4SS.

RESULTS AND DISCUSSION

VirB9^{CT} is only partially folded in solution but forms a tight and rigid complex upon binding to VirB7 (Souza et al., 2011). In order to solve the structure of VirB7-VirB9^{CT} and avoid aggregation due to oligomerization of VirB7 during our NMR studies, we used a peptide (VirB7^{NT}) corresponding to amino acids 24 to 46 (TKPAPDFGGRWKHVNHDFEAPTE) of the VirB7 N-terminal tail that contains the VirB9 binding site and mimics the interaction of full-length VirB7 with VirB9^{CT} (Souza et al., 2011). VirB7^{NT} binds to VirB9^{CT} in slow exchange at the NMR chemical shift timescale (Souza et al., 2011), with an apparent dissociation constant of 1 μ M as estimated by isothermal titration calorimetry (ITC) at 37°C (Table 1). ITC experiments carried out with full-length VirB7 yielded a similar dissociation constant (Table 1), indicating that the VirB7 C-terminal globular domain does not contribute significantly to the free energy of interaction between VirB7 and VirB9^{CT}. The VirB9^{CT}:VirB7^{NT} complex is mostly monomeric in solution (see below), as indicated by a mean isotropic overall rotational tumbling time of 6.6 ns (see Experimental Procedures) and a translational diffusion coefficient

of $11.04 \times 10^{-11} \text{ m}^2 \text{ s}^{-1}$ at 298 K. Both values are consistent with a 1:1 complex with a molecular weight of \sim 15 kDa. In agreement with previous observations (Souza et al., 2011), the ¹H-¹⁵N heteronuclear single quantum coherence (HSQC) spectrum of VirB9^{CT} recorded at 37°C displays fewer cross peaks than expected and a broad distribution of line widths, characteristic of a domain with significant conformational freedom (Figure 1B). In contrast, the ¹H-¹⁵N HSQC spectrum of ¹⁵N labeled VirB9^{CT} in the presence of the unlabeled VirB7^{NT} peptide displays the expected number of cross peaks and a narrower distribution of line widths (Figures 1B and S1), indicating that complex formation stabilizes a single VirB9^{CT} conformation. This finding is in marked contrast to the behavior of the TraO C-terminal domain (TraO^{CT}) in solution. TraO^{CT} is a VirB9^{CT} homolog from the conjugative plasmid pKM101, which is well structured even in the unbound state (Bayliss et al., 2007).

NMR Structure Calculation of the VirB7^{NT}-VirB9^{CT} Complex

In order to obtain detailed information about the interaction of Xac-VirB7 with Xac-VirB9, we solved the NMR structure of the VirB7^{NT}:VirB9^{CT} complex. Backbone resonance assignments (¹H^N, ¹⁵N, ¹³C α , ¹³C β , ¹³CO) were obtained for all residues of VirB9^{CT} (Figure S1), except for the amino acids belonging to the reminiscent purification tag, and for all the amino acids of VirB7^{NT} (only ¹H resonances) except for T²⁴ and T⁴⁵. The structure of the complex was calculated on the basis of 2,216 nuclear Overhauser effect (NOE) distance restraints obtained by semi-automated NOE assignment using CYANA 3.0, followed by water refinement using the RECCORD protocol (Nederveen et al., 2005). The precision of the final ensemble, consisting of the 20 lowest-energy NMR models, is given by a backbone root-mean-square deviation (RMSD) of 0.37 Å when the superposition is performed using both VirB9^{CT} residues 163–252 and VirB7^{NT} residues 30–38, or 0.32 Å and 0.41 Å when considering only VirB9^{CT} or VirB7^{NT} residues, respectively (Table 2). An analysis of the stereochemistry of the NMR models using Procheck (Laskowski et al., 1993) shows that all residues fall within the allowed regions of the Ramachandran plot (Table 2).

In order to validate the calculated structures, ¹H-¹⁵N residual dipolar couplings (D_{NH}) of VirB9^{CT} in complex with VirB7^{NT} were measured in the presence of a nematic phase of pentaethylene glycol monododecyl ether (C12E5) and n-hexanol ($r = 0.98$) (Rückert and Otting, 2000). The agreement between experimental and back-calculated residual dipolar couplings (RDCs) is given by a mean Q factor of 0.29 ± 0.01 for ¹H-¹⁵N spin pairs located within secondary structure elements (Figure S2; Table 2). As we lacked an ¹⁵N-labeled VirB7^{NT} peptide sample, D_{NH} values obtained for the full-length ¹⁵N-labeled VirB7 in complex with unlabeled VirB9^{CT} (Souza et al., 2011) were fitted using the coordinates of the bound conformation of the VirB7^{NT} peptide. A larger mean Q factor of 0.50 ± 0.17 was obtained (Figure S2; Table 2). This larger Q factor could, at least in part, be attributed to the lower precision of the RDC data, since the magnitude of the D_{NH} couplings measured along VirB7^{NT} (\sim 1–10 Hz) is smaller than for VirB9^{CT} (\sim –30 to 30 Hz) (Figure S2) and hence, more difficult to measure.

Table 2. Statistics of the NMR Structure Calculation

| | |
|---|------------------------|
| Completeness of Assignment ¹⁵ N- ¹³ C VirB9 ^{CT} : ¹⁴ N- ¹² C VirB7 ^{NT} (%) | 92.50 |
| Backbone VirB9 ^{CT} (¹⁵ NH, ¹³ Ca, ¹³ CO) (%) | 95.60 |
| Backbone VirB9 ^{CT} (¹ HN) (%) | 99.01 |
| Side-chain VirB9 ^{CT} (¹ H) (%) | 91.04 |
| Total VirB9 ^{CT} (¹ H, ¹⁵ N, ¹³ C) (%) | 93.26, 72.15, 84.86 |
| Backbone VirB7 ^{NT} (¹ HN) (%) | 94.74 |
| Side-chain VirB7 ^{NT} (¹ H) (%) | 90.22 |
| Total VirB7 ^{NT} (¹ H) (%) | 91.18 |
| Total Unambiguous Restraints | 2,216 |
| Unambiguous Restraints | |
| Intraresidual (i = j) | 535 |
| Sequential (i - j = 1) | 675 |
| Medium range (1 < i - j < 5) | 239 |
| Long range (i - j ≥ 5) | 767 |
| Intermolecular | 87 |
| Other Restraints | |
| TALOS ⁺ dihedral angles | 140 |
| Consistent Violations | |
| Distances >0.5 | 0 |
| Torsion angles >5° | 0 |
| RMSD from Mean (Å) | |
| All core residues (30–38, 163–252) | |
| All heavy atoms | 0.827 |
| Backbone atoms (N, C α , C') | 0.366 |
| VirB7 ^{NT} core residues (30–38) | |
| VirB7 ^{NT} heavy atoms | 1.119 |
| VirB7 ^{NT} backbone atoms (N, C α , C') | 0.415 |
| VirB9 ^{CT} core residues (163–252) | |
| VirB9 ^{CT} heavy atoms | 0.759 |
| VirB9 ^{CT} backbone atoms (N, C α , C') | 0.321 |
| Ramachandran Plot (30–38, 163–252) | |
| Most favored region (%) | 86.31 ± 2.51 |
| Additionally allowed region (%) | 12.36 ± 2.59 |
| Generously allowed region (%) | 1.32 ± 0.37 |
| Disallowed regions (%) | 0.00 ± 0.00 |
| WHAT CHECK Z Scores | |
| Ramachandran plot appearance | -2.42 ± 0.26 |
| Second-generation packing quality | 0.25 ± 0.28 |
| Chi1-Chi2 rotamer normality | -1.00 ± 0.35 |
| Backbone conformation | -4.23 ± 0.29 |
| G Factors | |
| Dihedrals | -0.26 ± 0.05 |
| Covalent | 0.11 ± 0.04 |
| Overall | -0.14 ± 0.03 |
| Q Factor from RDC Considering All NH in the Backbone of VirB9 ^{CT} | 0.57 ± 0.01 |
| Q Factor from RDC Considering the Rigid Conformation Parts of VirB9 ^{CT} | 0.29 ± 0.01 |

Table 2. Continued

| | |
|---|-------------|
| Q Factor from RDC of NHs with NOE-Het Higher than 0.5 in VirB7 ^{NT} | 0.50 ± 0.17 |
| BMRB Accession Number | 25512 |
| PDB ID | 2N01 |

VirB7^{NT} Folds into a Short β Strand upon Binding to VirB9^{CT}

VirB9^{CT} consists of a β sandwich formed by two β sheets, each containing four antiparallel β strands (Figure 2A). The first β sheet is composed of strands β 1 (residues 167–171), β 8 (residues 245–251), β 7 (residues 237–242), and β 4 (residues 206–210). The second β sheet is formed by strands β 2 (residues 182–186), β 3 (residues 189–193), β 6 (residues 228–232), and β 5 (residues 221–225). β strands 3 and 4 are connected by a well-defined loop, corresponding to residues 194–205 (loop 3), which contains a short 3_{10} helix (residues 196–198). Similarly, β strands 4 and 5 are connected by the well-defined loop 4 (residues 211–220) (Figure 2A). VirB7^{NT} folds into a short β strand, β 0 (residues 35 and 36), which contacts β 1 of VirB9^{CT} to form the 5-stranded antiparallel β sheet, β 0- β 1- β 8- β 7- β 4 (Figure 2A). As a means of further validating the conformation assumed by the VirB7^{NT} peptide in complex, we calculated the ¹H^N chemical shift differences between bound and free peptide and compared them with the chemical shift differences between bound and free full-length VirB7 (Figure S3). The downfield shifts observed for VirB7^{NT} residues K³⁵ and V³⁷ upon binding to VirB9^{CT} are consistent with hydrogen bond formation due to folding of a short β strand in this segment (Figure S3).

The side chain of VirB7^{NT} V³⁷ penetrates into the hydrophobic core of VirB9^{CT} between the two β sheets, making a series of hydrophobic contacts with the side chains of Y¹⁶⁷, Y¹⁶⁹, P¹⁸⁰, V¹⁸³, and L²⁴⁹ (Figures 2B and 2C). In addition, the aromatic side chains of F³⁰ and W³⁴ from VirB7^{NT} penetrate into a pocket located on the surface of the first β sheet of VirB9^{CT} (β 1- β 8- β 7- β 4), making contacts with the side chains of D¹⁶⁸, A¹⁷⁰, R²¹⁰, E²¹³, G²⁴⁸, and R²⁵⁰ (Figures 2B and 2C). These contacts could cause ring current effects involving the aromatic rings of F³⁰ and W³⁴, which could explain the unexpected chemical shifts observed for D¹⁶⁸, Y¹⁶⁹, A¹⁷⁰, and E²¹³ (Figure S4).

The general topology of the VirB7^{NT}-VirB9^{CT} complex is similar to that observed for the TraN:TraO^{CT} complex (PDB: 2OFQ) (Bayliss et al., 2007). The backbone RMSD between the secondary structure elements of the best NMR models of TraO^{CT}:TraN and VirB9^{CT}:VirB7^{NT} is 1.53 Å (Figure 3A). The most striking differences are found in the loops connecting the VirB9^{CT} β strands, the presence of an additional concave pocket on the surface of VirB9^{CT} and specific protein-peptide contacts (Figure 3). Specifically, loop 4 connecting β 4 and β 5 from VirB9^{CT} assumes a very different orientation, which is supported by a large number of intermolecular NOEs from F³⁰ (VirB7^{NT}) to E²¹³ and R²¹⁰ (VirB9^{CT}) (see below). The short β strand observed in loop 4 of TraO^{CT}:TraN is absent in the Xac VirB9^{CT}:VirB7^{NT} NMR structure (Figure 3). Differently from the TraO^{CT}:TraN complex, VirB7^{NT}:VirB9^{CT} lacks a 3_{10} helix in loop 1, but displays a short 3_{10} helix in loop 3 (Figures 2 and 3).

Despite the low level of amino acid sequence identity between TraO:TraN and VirB9:VirB7 (Figure 3B), most of the

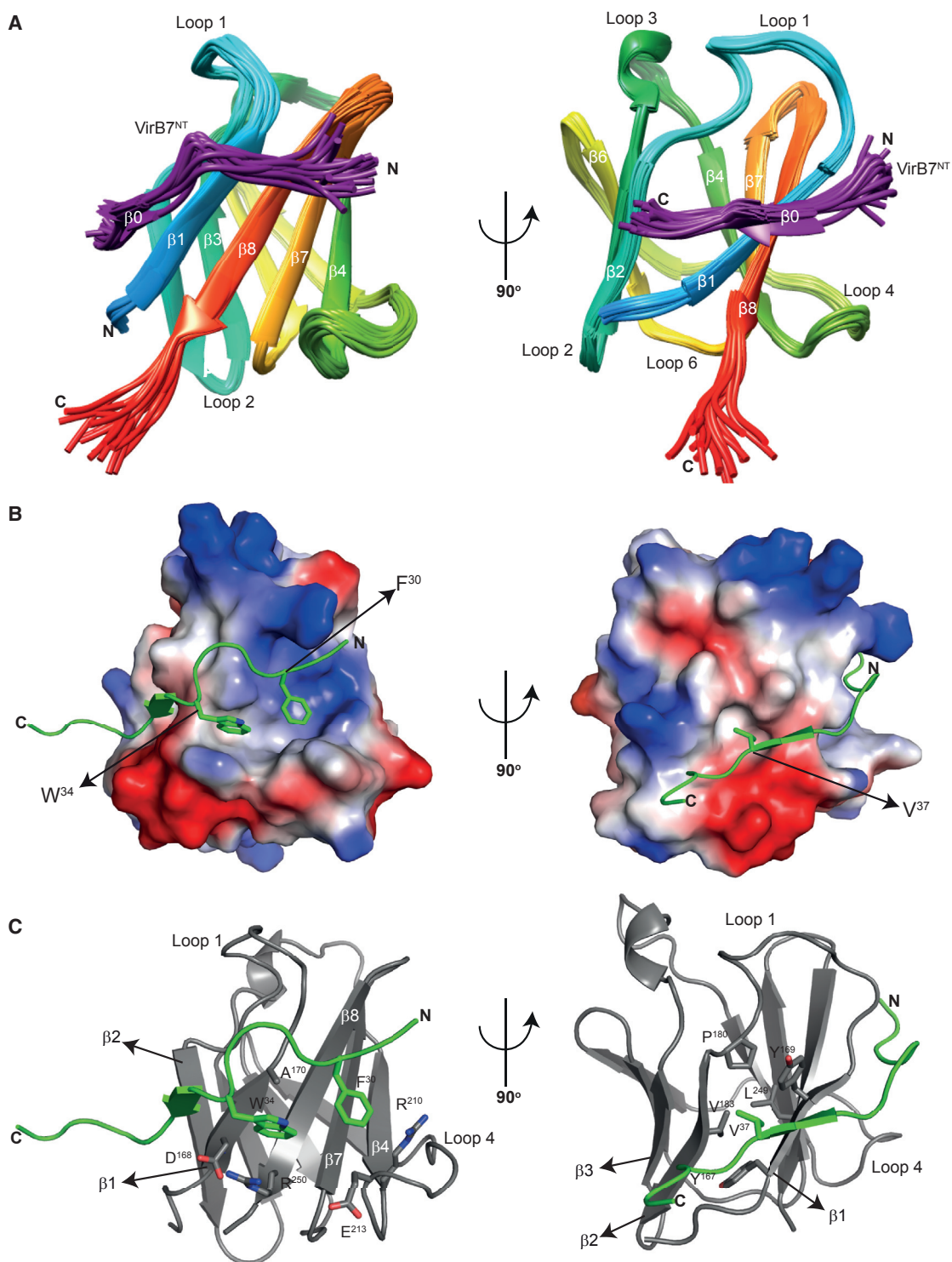


Figure 2. NMR Structure of the VirB9^{CT}:VirB7^{NT} Complex

(A) Backbone organization of the NMR ensemble consisting of the 20 lowest-energy models. Poorly defined regions (residues 154–162 and 253–255 of VirB9^{CT}, or 24–28 and 39–46 of VirB7^{NT}) are not shown. VirB7^{NT} is colored purple.

(B) Surface representation of the lowest-energy NMR model of VirB9^{CT} in complex with VirB7^{NT} (in cartoon) colored according to the electrostatic surface potential as calculated by PyMOL (Schrodinger, LLC). Red and blue colors indicate negative and positive potential energies, respectively.

(C) Cartoon representation of the lowest-energy NMR model showing intermolecular contacts made by VirB7^{NT} F³⁰, W³⁴, and V³⁷ (side chains shown as stick models). VirB9^{CT} is shown in gray and VirB7^{NT} is colored green.

See also Figures S2–S5.

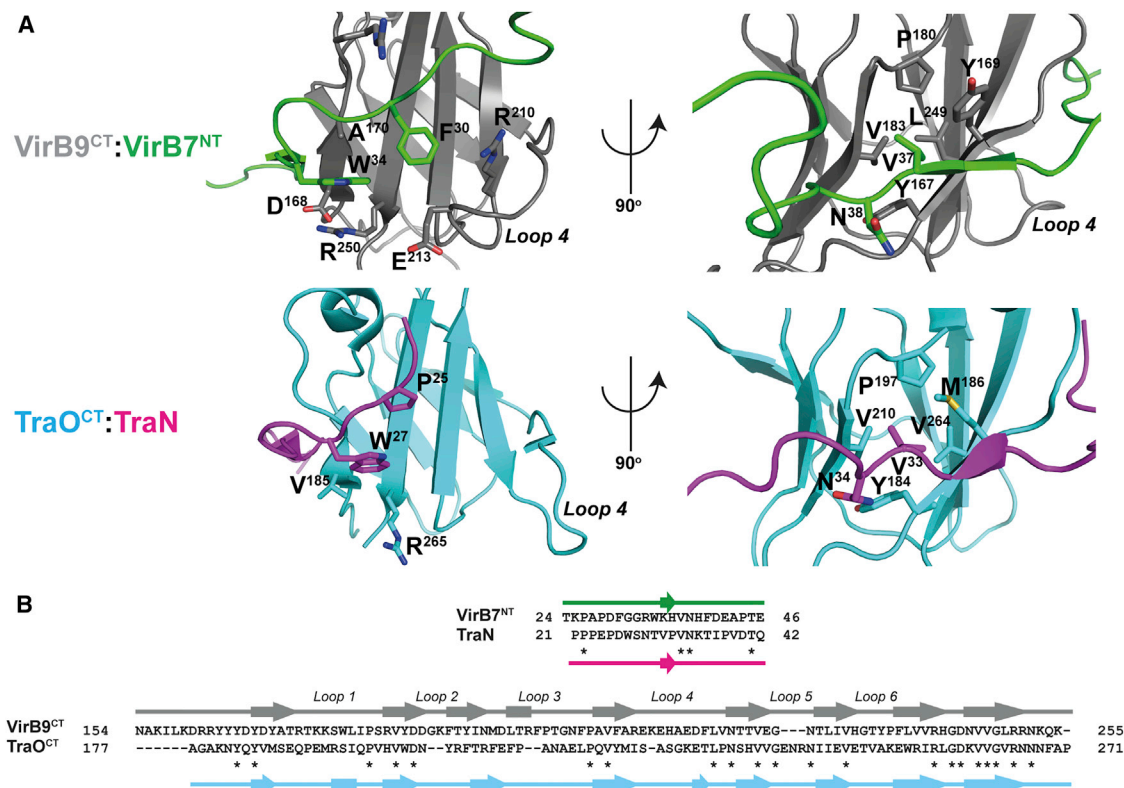


Figure 3. Comparison of VirB9^{CT}:VirB7^{NT} and TraO^{CT}:TraN Complexes

(A) Side chains that make intermolecular contacts in at least 80% of the VirB9^{CT}:VirB7^{NT} conformers are shown as sticks and compared with contacts between TraO and TraN (PDB: 2OFQ).

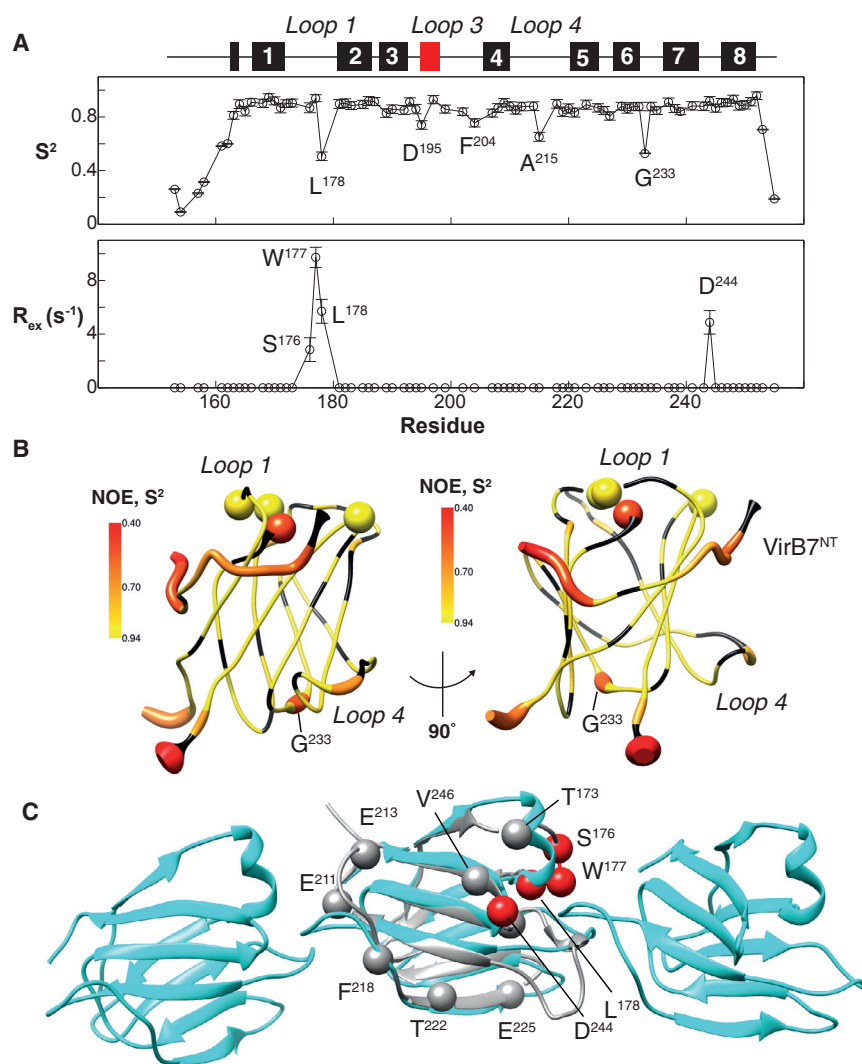
(B) Amino acid sequence alignments of TraN with VirB7^{NT} and of TraO^{CT} with VirB9^{CT}. Asterisks indicate identical residues. Secondary structure elements are indicated.

intermolecular interactions observed in the NMR structure of the TraO^{CT}:TraN complex are preserved in the complex between VirB9^{CT} and VirB7^{NT} (Figure 3). The motif P³²V³³N³⁴K³⁵ of TraN is conserved among orthologous proteins and was identified as being important for the interaction with TraO (Bayliss et al., 2007). The equivalent segment in Xac-VirB7 is H³⁶V³⁷N³⁸H³⁹ (Souza et al., 2011). Analogously to V³³ from TraO, V³⁷ of Xac VirB7 penetrates in the hydrophobic core of VirB9^{CT}, making several intermolecular interactions (Figures 3B and S5) as described above. Also, even though W³⁴ from VirB7^{NT} and W²⁷ from TraN do not occupy the same position in the amino acid sequence alignment (Figure 3), the two residues make similar intermolecular contacts with residues in β strands 1 and 8 of VirB9^{CT} and TraO^{CT}, respectively (Figure 3). It is noteworthy that W³⁴ in VirB7^{NT} makes a cation-pi interaction with R²⁵⁰ in VirB9^{CT}. This contact was observed in all calculated VirB7^{NT}:VirB9^{CT} conformers, but it is absent in the TraO^{CT}:TraN NMR structure where R²⁶⁵ assumes a different orientation (Figure 3). One of the largest differences between the binding interface of the two complexes is the presence of a phenylalanine (F³⁰) in VirB7 while a proline (P²⁵) is found at the equivalent position in the TraN:TraO^{CT} complex. F³⁰ lies over β 7 of VirB9^{CT} (Figure 2C), contacting E²¹³ (loop4), G²⁴⁸ (β 8), and the side chain of R²¹⁰ (Figure 3A). These interactions could be responsible for the different orientation of loop 4 in VirB9^{CT} relative to the orientation found

in TraO^{CT} (Figure 3). While the highly conserved N³⁴ of TraN is located between the two β sheets of the TraO^{CT} β sandwich, the equivalent residue of VirB7^{NT}, N³⁸, is oriented away from the VirB9^{CT} hydrophobic core and does not participate in intermolecular contacts in any of the conformers (Figure 3).

Backbone Dynamics

In order to characterize the backbone dynamics of VirB9^{CT} in complex with VirB7^{NT}, longitudinal (R_1) and transverse (R_2) ¹⁵N relaxation rates as well as the heteronuclear $\{^1\text{H}\}$ -¹⁵N NOE (het-NOE) were measured for ¹⁵N-labeled VirB9^{CT} in complex with unlabeled VirB7^{NT}. The relaxation data were analyzed using the extended model-free approach of Lipari and Szabo (1982) in order to calculate generalized order parameters (S^2) and internal correlation times (τ_i), which are measures of the amplitude and the rate of backbone motions at a given site. The profile of ¹⁵N order parameters along the backbone of VirB9^{CT} in complex with VirB7^{NT} is shown in Figures 4A and S6A and color-coded on the backbone of the complex (Figure 4B). VirB9^{CT} displays S^2 typical of a rigid protein with an average S^2 value of 0.8 (Figure 4A). Except for the N-terminal and the C-terminal tails, five other sites showed reduced S^2 values (lower than 0.80), namely L¹⁷⁸ in loop 1, D¹⁹⁵ and F²⁰⁴ in loop 3, A²¹⁵ in loop 4, and G²³³ in loop 6, indicating the presence of fast motions on the sub-nanosecond timescale (Figure 4). The



model-free analysis indicated the presence of relaxation caused by chemical exchange (R_{ex}) dynamics in loop 1 residues S¹⁷⁶, W¹⁷⁷, and L¹⁷⁸ as well as for D²⁴⁴ in the short β turn between strands $\beta 7$ and $\beta 8$. All these residues map to the same region on the surface of the structure (Figure 4B). It is interesting to note that the corresponding region of TraO is involved in TraO:TraO interactions within the crystal structure of the pKM101 core complex outer layer (Chandran et al., 2009) (Figure 4C). In order to understand whether the chemical exchange dynamics at S¹⁷⁶, W¹⁷⁷, L¹⁷⁸, and D²⁴⁴ could be explained by a weak dimerization of the VirB9^{CT}:VirB7^{NT} complex, we recorded ¹H-¹⁵N HSQC experiments in the range of 35–350 μ M complex (Figures S6B and S6C). Significant changes in the ¹H-¹⁵N chemical shifts with the protein concentration were detected for residues T¹⁷³, S¹⁷⁶, W¹⁷⁷, L¹⁷⁸, E²¹¹, E²¹³, F²¹⁸, T²²², E²²⁵, H²⁴², and V²⁴⁶. Superposition of the Xac-VirB9^{CT} NMR structure on the crystallographic coordinates of TraO^{CT} in the pKM101 tetradecamer show that, with the exception of T²²² and E²²⁵, all other residues could be located at the interface between two VirB9^{CT} subunits (Figure 4C). Therefore, the slow dynamics in the segment between S¹⁷⁶ and L¹⁷⁸ can be explained by transient dimerization

Figure 4. Backbone Dynamics of VirB9^{CT}:VirB7^{NT}

(A) ¹H-¹⁵N bond vector order parameters S^2 and exchange rates (R_{ex}) as a function of the VirB9^{CT} amino acid sequence. The positions of the secondary structure elements of VirB9^{CT} are shown at the top; the β strands are indicated by black rectangles and the 3_{10} helix by a red rectangle. The uncertainties in the internal mobility parameters (S^2 and R_{ex}) come from the fitting using TENSOR2.

(B) S^2 (VirB9^{CT}) or het-NOE (VirB7^{NT}) values are encoded in the color and thickness of the ribbon representation of the VirB9^{CT}:VirB7^{NT} complex. Residues with significant non-zero R_{ex} are shown as spheres. Regions for which no data are available are colored black. Some of the regions with low S^2 are indicated.

(C) The NMR structure of VirB9^{CT} (gray) was superimposed over one TraO^{CT} (cyan) subunit in a section of the pKM101 core complex crystal structure (PDB: 3JQO) in which TraF and TraN subunits were removed for clarity. Residues of VirB9^{CT} whose ¹H-¹⁵N chemical shifts significantly changed with the protein concentration (more than one SD above the mean) are indicated by spheres, and those that displayed non-zero R_{ex} are colored red.

See also Figure S6.

of the VirB9^{CT}:VirB7^{NT} complex in a head to tail fashion. This behavior could be mimicking the formation of a VirB9^{CT} ring around VirB10 subunits at the outer layer of the *Xanthomonas* T4SS core complex.

While the segment between VirB7^{NT} D²⁹ and N³⁸ of VirB7^{NT} is well defined, the NMR structure displays lower precision at its N- and C-terminal tails (residues

24–28 and 39–46) (Figure 2). To assess the correlation between VirB7 internal dynamics and the precision of the current NMR ensemble along the peptide backbone, we re-analyzed ¹⁵N relaxation data obtained for the full-length ¹⁵N-VirB7 in complex with unlabeled VirB9^{CT} (Souza et al., 2011) in light of our current structural data. When color-coded on the structure of VirB7^{NT} in complex (Figure 4B), het-NOE values obtained for the full-length VirB7 bound to VirB9^{CT} show that the well-defined segment between W³⁴ and V³⁷ displays restricted dynamics in comparison with the tails. Thus, our findings showing a short β strand flanked by more flexible regions in VirB7^{NT} are consistent with both the internal dynamics and the ¹H^N chemical shift changes of the full-length protein upon complex formation (Figure S3).

Specific Intermolecular Contacts Are Critical Determinants of VirB7^{NT}:VirB9^{CT} Complex Stability

To assess the contribution of specific intermolecular interactions to the stability of the VirB7^{NT}:VirB9^{CT} complex, dissociation constants (K_d) for complexes formed by VirB9^{CT} and wild-type (WT) or mutant VirB7^{NT} peptides were determined by ITC or NMR titration experiments (Table 1 and Figures S7 and S8).

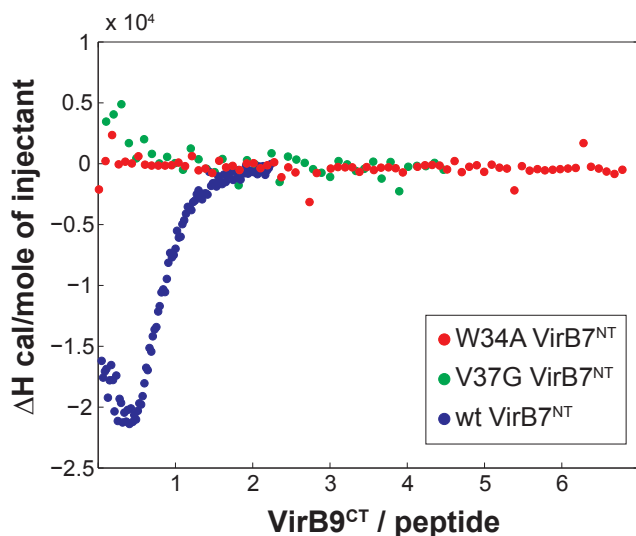


Figure 5. ITC Measurements Indicate that W³⁴ and V³⁷ Are Critical Determinants of the Binding Affinity between VirB7^{NT} and VirB9^{CT}

ITC measurements of VirB7^{NT} WT (dark blue), V37G (green), and W34A (red) mutants with VirB9^{CT}.

See also Figures S7 and S8.

Substitution of VirB7^{NT} W³⁴ for an alanine or of VirB7^{NT} V³⁷ for a glycine reduced the binding affinity to undetectable levels (Figure 5, Table 1). Consistent with the ITC results, NMR titrations showed that substitution of VirB7^{NT} W³⁴ completely abolishes the interaction between VirB7^{NT} and VirB9^{CT}, while the V37G mutant peptide still binds to VirB9^{CT} in slow exchange at the NMR timescale, albeit with a much greater apparent K_d (Table 1, Figure S8). When V³⁷ is replaced by an alanine instead of a glycine, the binding free energy is partially restored (Table 1). When V³⁷ is replaced by a phenylalanine, the K_d changes slightly compared with WT VirB7^{NT} (2.5 μ M versus 1 μ M; Table 1), indicating that other bulky side chains can be fairly accommodated in the hydrophobic core of VirB9^{CT}. Substitution of F³⁰ to alanine increases the K_d from 1 μ M to 6.6 μ M, perhaps due to a reduced number of intermolecular contacts with VirB9^{CT}. The substitution of other VirB7^{NT} residues at the interface with VirB9^{CT}, such as D²⁹ and N³⁸, increases the K_d to 4.1 or 6.1 μ M, respectively (Table 1). Similarly to F³⁰, these residues contribute modestly to the stability of the complex in comparison with W³⁴ and V³⁷.

Specific VirB7:VirB9 and VirB7:VirB7 Interactions Are Critical for T4SS Assembly and Activity In Vivo

As a means of assessing the importance of the interactions between VirB7 and VirB7, and between VirB7 and VirB9 on the activity of Xac's T4SS, Xac cells carrying a deletion of the *virB7* gene were complemented with plasmids harboring mutant *virB7* genes (Figure 6A) whose expression is under the control of an arabinose-inducible promoter. In *Xanthomonas* cells, this promoter has a low basal expression level in the absence of arabinose, while a very strong activity is shown under inducing conditions (see below). We used these altered gene expression levels to vary the amount of cellular VirB7. The Xac strains carrying *virB7* variants were then used in growth competition assays

against *Escherichia coli* cells and in western blot assays to compare intracellular levels of VirB7 and VirB9 proteins.

When *virB7* is deleted from the genome (Δ B7), Xac cells lose T4SS-dependent bacterial killing activity as has been previously shown (Figure 6B; Souza et al., 2015). Complementation with a plasmid harboring the WT *virB7* gene (Δ B7cWT) under VirB7-inducing conditions restores the antibacterial activity to levels similar to those observed for the WT strain (Figure 6B). In contrast, complementing the *virB7* knockout strain with the *virB7* W34A mutant (Δ B7cW34A) does not restore Xac's competitiveness to the same level as observed in the strain complemented with the WT *virB7* (Figure 6B). Nevertheless, complementation with the *virB7* V37G mutant (Δ B7cV37G) restores Xac's competitiveness in the presence of inducer to almost the same level as the mutant strain complemented with the WT *virB7* (Figure 6B). To assess whether VirB7 and VirB9 proteins are present in the Δ B7cW34A and Δ B7cV37G strains, western blotting was performed using antibodies against both proteins under inducing conditions. A small amount of VirB9 was detected in the total cellular fraction of Xac cells complemented with the plasmid expressing *virB7*-V37G but not with the plasmid expressing *virB7*-W34A (Figure 6C).

In order to evaluate if the expression level of VirB7 could influence VirB9 levels, the competition and the western blotting experiments were repeated using cells cultivated in the absence of arabinose, thus allowing for basal gene expression (Figure S9). In this case, the mutant *virB7*-V37G does not restore the bactericidal activity of the T4SS (Figure S9A), nor is VirB9 detected in these cells (Figure S9B). The fact that VirB9 is not detected (Figure S9B) suggests that it is degraded, possibly due to its greater conformational freedom when not bound to VirB7 (Figure 1) and, consequently, the T4SS channel is not assembled. This conclusion is supported by previous experiments showing that, in *Xanthomonas* cells, VirB9 and VirB10 are not detected in the absence of VirB7 (Souza et al., 2011). The detection of a small amount of VirB9 in the cells grown in the presence of arabinose (Figure 6C) could be attributed to the greater expression level of the VirB7 V37G mutant achieved by the action of the inducer that could compensate for its lower binding affinity relative to the WT (Table 1). In summary, the W34A mutation abolishes the binding of VirB7 to VirB9 in vitro and in vivo, while binding may still be detected for the V37G mutant when its expression level is increased (Table 1; Figures 6C and S9). Our findings show a clear correlation between reduced antibacterial activity and decreased in vitro affinity for these mutants. We conclude that the disruption of the VirB7-VirB9^{CT} complex prevents the assembly of the T4SS, which ultimately causes loss of bacterial killing activity.

VirB7 Oligomerization Is Required for T4SS Killing Activity

As mentioned above, VirB7 proteins from the Xanthomonadaceae family of bacteria contain an additional N0 C-terminal domain (residues 52–133, VirB7^{CT} in the Xac protein), which is absent in the VirB7 proteins of most other T4SSs. VirB7^{CT} does not interact with VirB9 but recognizes residues 42–49 of the VirB7 unfolded N-terminal tail (Figure 6A). These VirB7-VirB7 interactions potentially organize the N0 domains around the external perimeter of the *Xanthomonas* T4SS core complex

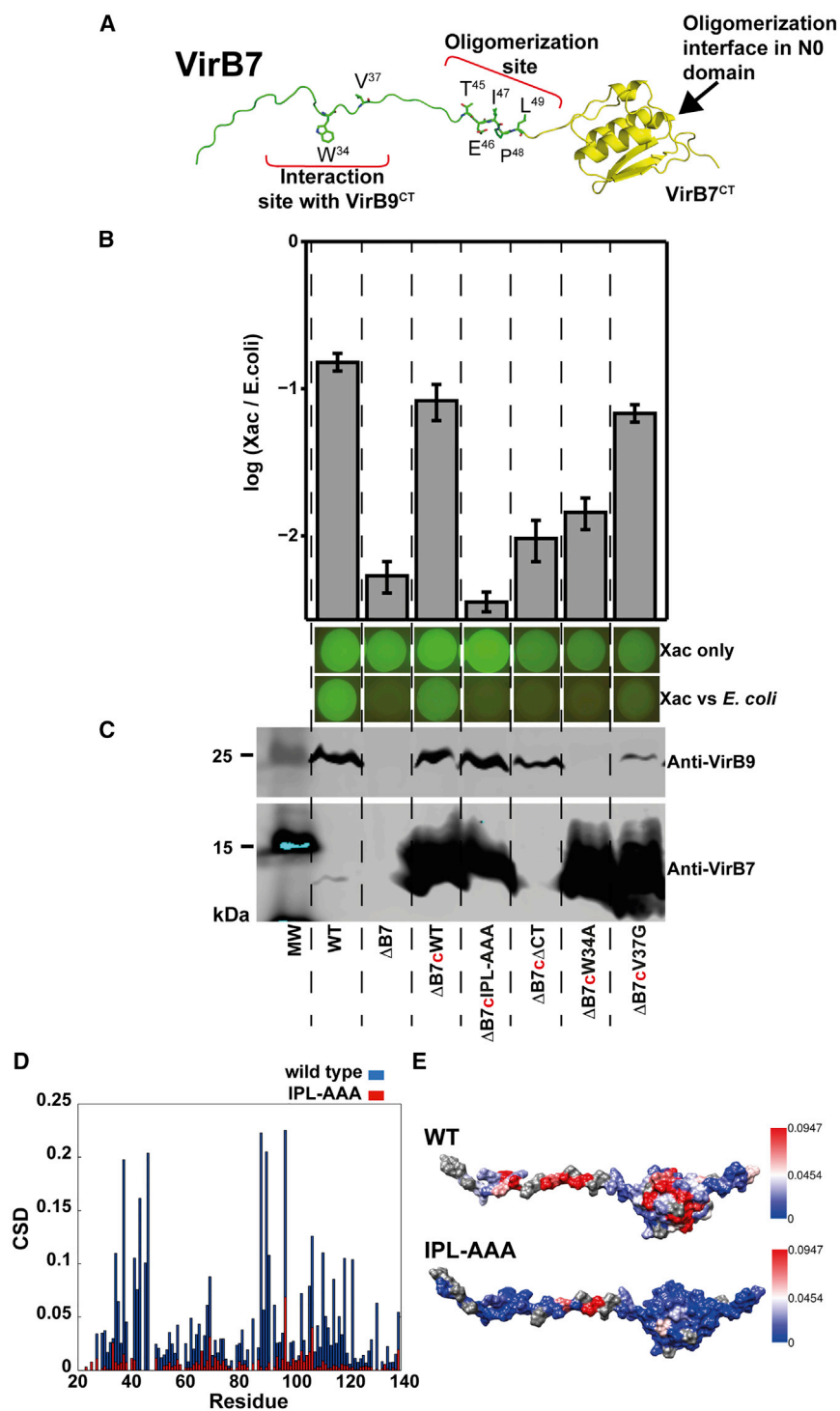


Figure 6. VirB7:VirB7 and VirB7:VirB9 Inter-molecular Interactions Are Critical for the Bactericidal Function of the *Xanthomonas* T4SS

(A) VirB7 NMR structure (PDB: 2L4W) showing the interaction site with VirB9^{CT} in the N-terminal tail and VirB7-VirB7 oligomerization sites in the N-terminal disordered region and in the C-terminal globular domain.

(B) Ratio of the number of *Xac* and *E. coli* cells after interbacterial competition experiments performed under VirB7-inducing conditions (Top). Colonies of *Xac* cells expressing GFP visualized after cell growth in the presence or absence of non-fluorescent *E. coli* (bottom). Error bars represent the standard deviation of four experiments.

(C) Western blotting showing the VirB7 and VirB9 levels in *Xac* strains grown in the presence of arabinose inducer. Primary antibodies are indicated on the right. *Xac* strains used are indicated below each lane (complemented strains are indicated with a red "c"). MW, molecular weight marker. Mature VirB7 and VirB9, after the removal of their signal peptides have a molecular weight of 12.6 and 26.6 kDa, respectively. The VirB7 protein was not detected in the $\Delta B7c\Delta CT$ strain because it expresses a mature VirB7 variant with a molecular weight of 3.1 kDa. Experiments similar to those shown in (B and C) performed in the absence of VirB7 overexpression are shown in Figure S9.

(D) Chemical shift differences (CSDs) observed for WT VirB7 (blue) and the VirB7^{IPL-AAA} mutant (red) upon increasing the protein concentration from 50 μ M to 300 μ M.

(E) Residues displaying chemical shift differences greater than the mean plus 1 SD are color-coded red. Unassigned residues are shown in gray. See also Figure S9.

that interacts with VirB9 is sufficient for the stable assembly of the *Xac* T4SS core complex but is not sufficient for its proper function.

In order to further study the importance of VirB7 oligomerization for *Xac* T4SS function, residues I⁴⁷P⁴⁸L⁴⁹, located at the VirB7 oligomerization interface in its N-terminal tail (Figure 6A), were substituted by alanines, generating the triple mutant VirB7^{IPL-AAA}. The purified recombinant protein, in contrast to WT VirB7, does not oligomerize in vitro as indicated by translational diffusion coefficients (D_t) and overall rotational tumbling

(Souza et al., 2011). In order to assess the functional relevance of the VirB7^{CT}, we investigated whether its complete removal would alter *Xac* T4SS bacterial killing activity. Indeed, complementation of *Xac virB7* knockout cells with *virB7* Δ CT does not restore the T4SS bacterial killing activity (Figure 6B). However, we were able to detect the VirB9 protein by western blot analysis in the *Xac virB7* knockout cells complemented with *virB7* Δ CT (Figure 6C). This suggests that the VirB7 N-terminal domain

times (τ_c) measured by NMR (Table 3). This conclusion is confirmed by the observation that while the WT VirB7 protein displays significant concentration-dependent chemical shift perturbations due to oligomerization, these perturbations are not observed for the VirB7^{IPL-AAA} protein (Figures 6D and 6E). It is worth noting that VirB7^{IPL-AAA} is well folded as the ¹H-¹⁵N chemical shifts of globular domain residues not involved in oligomerization are essentially identical to that of the WT VirB7. We

Table 3. Isotropic Overall Rotational Tumbling Times, τ_c , and Translational Diffusion Coefficients, D_t , Measured for the WT VirB7 and the VirB7^{IPL-AAA} Mutant at Two Different Protein Concentrations

| VirB7 (Concentration, μM) | τ_c (ns) | D_t ($\text{m}^2 \text{s}^{-1} \times 10^{-11}$) |
|---------------------------------------|---------------|--|
| WT (50) | 7.91 | 8.40 \pm 0.40 |
| WT (300) | 12.56 | 7.28 \pm 0.12 |
| IPL-AAA (50) | 7.92 | 9.33 \pm 0.19 |
| IPL-AAA (300) | 7.86 | 8.84 \pm 0.85 |

then tested whether this mutant could recover VirB7 function in the ΔvirB7 mutant strain. Figure 6B shows that the $\text{virB7}^{\text{IPL-AAA}}$ gene is unable to restore T4SS-dependent killing activity, even when this protein is overexpressed. These results demonstrate that the VirB7-VirB7 interaction is functionally relevant. Interestingly, Xac virB7 knockout cells expressing VirB7^{IPL-AAA} produce VirB9 protein at the same level as the WT strain (Figures 6C and S9B). This confirms that, even without VirB7 oligomerization, the VirB7-VirB9 complex is formed, and that VirB9 is stabilized in this strain. Therefore, the results clearly indicate that VirB7-VirB7 oligomerization is essential for proper T4SS function, although it does not seem to be absolutely necessary for T4SS biogenesis or stability. Thus, the presence of VirB7^{NT} and its binding to VirB9 are required and sufficient for the stabilization of the core complex.

In summary, the N-terminal domain of VirB7 from *Xanthomonas citri*'s bactericidal T4SS folds into a short β strand and complements a β sheet in the VirB9 C-terminal domain in a manner similar to that observed for the homologous TraN/TraO complex from the *E. coli* conjugative plasmid pKM101. In contrast to TraN/TraO, binding to VirB7 is responsible for a large structural stabilization of the VirB9 C-terminal domain. Disruption of the Xac VirB7-VirB9 complex prevents the assembly of the T4SS in vivo, causing loss of antibacterial activity. This observation could be explained by the significant increase in conformational stability of VirB9 upon binding to VirB7. We showed previously that Xac VirB7 has an extra C-terminal N0 domain (VirB7^{CT}) involved in VirB7 oligomerization in vitro. This suggested that the VirB7^{CT} could form an extra symmetric ring around the core complex outer layer of Xac T4SS, a significant structural difference with respect to T4SSs encoded by the *E. coli* conjugative plasmids pKM101 and R388 (Fronzes et al., 2009; Low et al., 2014). Disruption of the VirB7-VirB7 self-association interface or deletion of VirB7's N0 domain does not seem to prevent the assembly of the T4SS, but the higher-order oligomerization of VirB7 is required for *Xanthomonas* T4SS function. In conclusion, a functional bacterial killing T4SS requires not only the formation of a stable core complex but also the oligomerization of VirB7 around the outer layer of the core complex. These findings may be relevant for other T4SSs with similar architecture, such as the type IVB secretion systems found in the human pathogens *Legionella pneumophila* and *Coxiella burnetii* (Kubori and Nagai, 2015) (Nakano et al., 2010) (Zamboni et al., 2003).

EXPERIMENTAL PROCEDURES

Gene Cloning, Protein Production, and Purification

A complete description of gene cloning, production, and purification of the constructs used in this work can be found in the Supplemental Information.

NMR Spectroscopy

NMR experiments were performed on Bruker Avance III spectrometers operating at 500 and 800 MHz (University of São Paulo), and 900 MHz (University of Utrecht), and on an Agilent instrument operating at 600 MHz (Brazilian Biosciences National Laboratory). All instruments (except 500 MHz) were equipped with cryogenic probes. The experiments were performed at 37°C. NMR samples of the 1:1 complex consisted of approximately 500 μM of ¹⁵N, ¹³C-VirB9^{CT} and unlabeled VirB7^{NT} dissolved in 20 mM deuterated sodium acetate (pH 5.0), containing 50 mM NaCl, 0.5 mM TSP, 0.05% (w/v) Na₂S₂O₃, and 10% (v/v) D₂O. NMR spectra were processed with NMRPipe (Delaglio et al., 1995) and analyzed with CcpNmr Analysis (Vranken et al., 2005). VirB9^{CT} backbone resonances were assigned using HNCA, HN(CO)CA, HNCACB, CBCA(CO)NH, HNCO, and HN(CA)CO. Side-chain resonances were assigned with (H)CCH-total correlation spectroscopy (TOCSY), H(C)CH-TOCSY, H(CCO)NH-TOCSY, ¹⁵N-TOCSY-HSQC, ¹³C HSQC-NOE spectroscopy (NOESY), and for the aromatics, additional 2D (HB)CB(CGCD)HD and (HB)CB(CGCDCE)HE. Proton resonances for VirB9^{CT}-bound VirB7^{NT} were assigned using 2D ¹H-¹H TOCSY and 2D-NOE experiments acquired with double filters for ¹⁵N and ¹³C. Backbone and side-chain resonance chemical shift assignments for VirB9^{CT} and VirB7^{NT} were deposited in the BMRB (BMRB: 25512).

Titrations of unlabeled WT or V37G VirB7^{NT} mutant into a solution of 275 μM ¹⁵N-VirB9^{CT} were monitored by ¹H-¹⁵N-HSQC experiments. The NMR titration curves obtained for the WT VirB7^{NT} and VirB7^{NT} V37G mutant (Figure S8) were analyzed using the binding polynomial formalism and assuming a 1:1 stoichiometry. Since the NMR binding curves were noisy, this analysis provided a first estimate for the K_d , which for the WT VirB7^{NT} is of the same order of magnitude as the K_d value obtained by ITC (Table 1).

Descriptions of the methods used for measuring ¹⁵N relaxation rates, ¹H-¹⁵N RDCs, chemical shift differences, and the diffusion-ordered NMR spectroscopy experiments are available as Supplemental Information.

Structure Determination

NMR structure calculations and automated NOE assignments were performed using the CYANA 3.0 software (Güntert et al., 1997; Herrmann et al., 2002). NOEs were collected from 3D NOESY-¹H-¹⁵N]-HSQC, 3D NOESY-¹H-¹³C]-HSQC recorded separately for aliphatic and aromatic ¹³C resonances, 2D-NOESY, 2D ¹⁵N/¹³C double-filtered NOE and 3D HCN-NOESY (Diercks et al., 1999) spectra and used as ambiguous input in CYANA in addition to chemical shifts of assigned resonances, manually assigned NOE peaks, and Talos+-predicted (Shen and Bax, 2013), chemical-shift-derived ϕ and ψ angles. Intermolecular and intramolecular hydrogen bond restraints were generated based on their consistent presence in structure ensembles of preliminary calculations and used as input in the final calculation. The final distances, dihedral angles, and hydrogen bond restraints generated by CYANA were used as input for a recalculation step in CNS (Brünger et al., 1998), followed by a final refinement in explicit water using the RECOORD scripts (Nederveen et al., 2005). The 20 lowest-energy structures obtained after the water refinement were deposited in the PDB (PDB: 2N01).

Isothermal Titration Calorimetry

Isothermal titration calorimetry was performed on a VP-ITC microcalorimeter (MicroCal). All solutions were degassed prior to the experiments. The titration cell was filled with ca. 1.8 mL of a 10–20 μM VirB7^{NT} peptide solution or full-length VirB7 (Table S3). The injection syringe was filled with VirB9^{CT} at concentrations of 200–600 μM (Table S3). Protein and peptide samples were dissolved using the same sodium acetate solution 20 mM at pH 5.0 containing 100 mM NaCl. A control experiment was performed when the buffer was titrated against the peptide, and another control experiment was performed when the protein was titrated against the buffer. The analysis was performed after subtraction of the control curves from the experiment. All experiments were repeated at least twice, and the reported uncertainties were derived from the fitting. ITC data were analyzed using the program OriginLab 7.0 (OriginLab Corporation).

Interbacterial Growth Competition Experiments

Xac cells expressing GFP through the plasmid pBBR5-GFP (strains: WT, ΔB7 , ΔB7cWT , ΔB7cIPL , $\Delta\text{B7c}\Delta\text{CT}$, $\Delta\text{B7cW34A}$, and $\Delta\text{B7cV37G}$) (Table S4), and the non-fluorescent *E. coli* BL21(DE3)RIL ArcticExpress were grown in 2 \times TY medium until the exponential phase ($\text{OD}_{600} = 1.0$). Cells were washed and

resuspended to achieve an OD₆₀₀ of 2.0 for Xac and 0.2 for *E. coli*. Xac cells were then mixed with *E. coli* (Xac:*E. coli*) to a final ratio of 10:1. The mixtures were pipetted onto Luria-Bertani (LB) agar plates supplemented with spectinomycin (100 µg/mL) and gentamicin (20 µg/mL) either in the presence or in the absence of 0.3% (w/v) L(+)-arabinose. Competitions were carried out at 30°C for 48 hr and evaluated by determining the CFU (colony forming unity) of each strain (Souza et al., 2015). In order to quantitatively estimate the ratio between Xac and *E. coli* cells, the colonies were excised from the plates and transferred to 1 mL of 2× TY medium. Aliquots from a serial dilution were taken and cultivated in LB agar plates supplemented with 150 µg/mL ampicillin or 15 µg/mL tetracycline for selection of Xac (ampicillin resistant) or *E. coli* cells (tetracycline resistant). The CFU were counted after 12 hr (*E. coli*) or 36 hr (Xac) incubation at 30°C.

Western Blotting

Xac strains were cultivated for 12 hr in 4 mL of 2× TY supplemented with 150 µg/mL ampicillin either in the presence or in the absence of 0.3% (w/v) of L(+)-arabinose. Western blots of total cellular fractions were carried out using the primary antibodies against VirB7 and VirB9 (Souza et al., 2011) at 1:2,000 dilutions. The primary antibodies were detected using IRDye 800CW goat anti-rabbit IgG (LI-COR Biosciences) at a 1:25,000 dilution. Nitrocellulose membranes were scanned using an Odyssey CLx infrared imaging system (LI-COR Biosciences).

ACCESSION NUMBERS

The accession numbers for the VirB7 and VirB9 sequences reported in this paper are Genbank: AAM37471.1, AAM37469.1. The accession numbers for the structure coordinates and for the NMR data are PDB 2N01 and BMRB 25512.

SUPPLEMENTAL INFORMATION

Supplemental Information includes Supplemental Experimental Procedures, nine figures, four tables, and one pdb file and can be found with this article online at <http://dx.doi.org/10.1016/j.str.2016.07.015>.

AUTHOR CONTRIBUTIONS

Conceived and designed the experiments: D.P.S., R.K.S., and C.S.F. Performed NMR experiments: L.C.O., D.P.S., D.C.F., H.W., R.B., and R.K.S. Structure calculations: L.C.O., H.W., and R.K.S. Cloning: D.P.S. and L.C.O. Interbacterial competition experiments: L.C.O. and G.U.O. ITC experiments: L.C.O. and F.S.L. Analyzed the data: L.C.O., D.P.S., G.U.O., R.J.O., H.W., R.B., C.S.F., and R.K.S. Wrote the paper: L.C.O., R.K.S., D.P.S., and C.S.F.

ACKNOWLEDGMENTS

We thank Dr. Clemens Anklin (Bruker BioSpin) for support on the acquisition of the double-filtered NMR experiments, Dr. A.C. Zeri and M. Sforça for support on the use of the Agilent 600 MHz NMR instrument, and J. Vilcachagua for support on the use of the Bruker 500 MHz NMR instrument. We thank Dr. Hugo van Ingen for discussions and support during the structure calculations. This work was supported by funds from FAPESP (Brazil) to C.S.F. (2011/07777-5) and to R.K.S. (2013/17883-2), and FAPEMIG to R.J.O. L.C.O. and G.U.O. acknowledge PhD fellowships from CNPq and CAPES (Brazil). D.P.S. acknowledges postdoctoral fellowships from FAPESP and CAPES. F.S.L. acknowledges a FAPESP postdoctoral fellowship. L.C.O. received a travel award for a three-month stay at Utrecht University from the European Union (BioNMR, 261863). R.J.O. thanks GridUnesp for the computational resources.

Received: April 17, 2016

Revised: July 19, 2016

Accepted: July 22, 2016

Published: September 1, 2016

REFERENCES

Alegria, M.C., Souza, D.P., Andrade, M.O., Docena, C., Khater, L., Ramos, C.H.I., da Silva, A.C.R., and Farah, C.S. (2005). Identification of new protein-

protein interactions involving the products of the chromosome- and plasmid-encoded type IV secretion loci of the phytopathogen *Xanthomonas axonopodis* pv. *citri*. *J. Bacteriol.* *187*, 2315–2325.

Alvarez-Martinez, C.E., and Christie, P.J. (2009). Biological diversity of prokaryotic type IV secretion systems. *Microbiol. Mol. Biol. Rev.* *73*, 775–808.

Bayliss, R., Harris, R., Coutte, L., Monier, A., Fronzes, R., Christie, P.J., Driscoll, P.C., and Waksman, G. (2007). NMR structure of a complex between the VirB9/VirB7 interaction domains of the pKM101 type IV secretion system. *Proc. Natl. Acad. Sci. USA* *104*, 1673–1678.

Brünger, A.T., Adams, P.D., Clore, G.M., DeLano, W.L., Gros, P., Grosse-Kunstleve, R.W., Jiang, J.S., Kuszewski, J., Nilges, M., Pannu, N.S., et al. (1998). Crystallography & NMR system: a new software suite for macromolecular structure determination. *Acta Crystallogr. D Biol. Crystallogr.* *54*, 905–921.

Brunings, A.M., and Gabriel, D.W. (2003). *Xanthomonas citri*: breaking the surface. *Mol. Plant Pathol.* *4*, 141–157.

Büttner, D., and Bonas, U. (2010). Regulation and secretion of *Xanthomonas* virulence factors. *FEMS Microbiol. Rev.* *34*, 107–133.

Chandran, V., Fronzes, R., Duquerroy, S., Cronin, N., Navaza, J., and Waksman, G. (2009). Structure of the outer membrane complex of a type IV secretion system. *Nature* *462*, 1011–1015.

Costa, T.R.D., Felisberto-Rodrigues, C., Meir, A., Prevost, M.S., Redzej, A., Trokter, M., and Waksman, G. (2015). Secretion systems in Gram-negative bacteria: structural and mechanistic insights. *Nat. Rev. Microbiol.* *13*, 343–359.

Das, A.K. (2003). Citrus canker - a review. *J. Appl. Hort.* *5*, 52–60.

Delaglio, F., Grzesiek, S., Vuister, G.W., Zhu, G., Pfeifer, J., and Bax, A. (1995). NMRPipe: a multidimensional spectral processing system based on UNIX pipes. *J. Biomol. NMR* *6*, 277–293.

Diercks, T., Coles, M., and Kessler, H. (1999). An efficient strategy for assignment of cross-peaks in 3D heteronuclear NOESY experiments. *J. Biomol. NMR* *15*, 177–180.

Fronzes, R., Schäfer, E., Wang, L., Saibil, H.R., Orlova, E.V., and Waksman, G. (2009). Structure of a type IV secretion system core complex. *Science* *323*, 266–268.

Güntert, P., Mumenthaler, C., and Wüthrich, K. (1997). Torsion angle dynamics for NMR structure calculation with the new program Dyana1. *J. Mol. Biol.* *273*, 283–298.

Herrmann, T., Güntert, P., and Wüthrich, K. (2002). Protein NMR structure determination with automated NOE assignment using the new software CANDID and the torsion angle dynamics algorithm DYANA. *J. Mol. Biol.* *319*, 209–227.

Ilangoan, A., Connery, S., and Waksman, G. (2015). Structural biology of the Gram-negative bacterial conjugation systems. *Trends Microbiol.* *23*, 301–310.

Kaplan, M., Cukkemane, A., van Zundert, G.C.P., Narasimhan, S., Daniëls, M., Mance, D., Waksman, G., Bonvin, A.M.J.J., Fronzes, R., Folkers, G.E., et al. (2015). Probing a cell-embedded megadalton protein complex by DNP-supported solid-state NMR. *Nat. Methods* *12*, 649–652.

Kubori, T., and Nagai, H. (2015). The Type IVB secretion system: an enigmatic chimera. *Curr. Opin. Microbiol.* *29*, 22–29.

Laskowski, R.A., MacArthur, M.W., Moss, D.S., and Thornton, J.M. (1993). PROCHECK: a program to check the stereochemical quality of protein structures. *J. Appl. Crystallogr.* *26*, 283–291.

Lipari, G., and Szabo, A. (1982). Model-free approach to the interpretation of nuclear magnetic resonance relaxation in macromolecules. 1. Theory and range of validity. *J. Am. Chem. Soc.* *104*, 4546–4559.

Low, H.H., Gubellini, F., Rivera-Calzada, A., Braun, N., Connery, S., Dujeancourt, A., Lu, F., Redzej, A., Fronzes, R., Orlova, E.V., et al. (2014). Structure of a type IV secretion system. *Nature* *508*, 550–553.

Mansfield, J., Genin, S., Magori, S., Citovsky, V., Sriariyanum, M., Ronald, P., Dow, M., Verdier, V., Beer, S.V., Machado, M.A., et al. (2012). Top 10 plant pathogenic bacteria in molecular plant pathology. *Mol. Plant Pathol.* *13*, 614–629.

Nakano, N., Kubori, T., Kinoshita, M., Imada, K., and Nagai, H. (2010). Crystal structure of Legionella DotD: insights into the relationship between type IVB and type II/III secretion systems. *PLoS Pathog.* *6*, e1001129.

- Nederveen, A.J., Doreleijers, J.F., Vranken, W., Miller, Z., Spronk, C.A.E.M., Nabuurs, S.B., Güntert, P., Livny, M., Markley, J.L., Nilges, M., et al. (2005). RECOORD: a recalculated coordinate database of 500+ proteins from the PDB using restraints from the BioMagResBank. *Proteins* 59, 662–672.
- Rivera-Calzada, A., Fronzes, R., Savva, C.G., Chandran, V., Lian, P.W., Laeremans, T., Pardon, E., Steyaert, J., Remaut, H., Waksman, G., et al. (2013). Structure of a bacterial type IV secretion core complex at subnanometre resolution. *EMBO J.* 32, 1195–1204.
- Rückert, M., and Otting, G. (2000). Alignment of biological macromolecules in novel nonionic liquid crystalline media for NMR experiments. *J. Am. Chem. Soc.* 122, 7793–7797.
- Ryan, R.P., Vorhölter, F.-J., Potnis, N., Jones, J.B., Van Sluys, M.-A., Bogdanove, A.J., and Dow, J.M. (2011). Pathogenomics of *Xanthomonas*: understanding bacterium–plant interactions. *Nat. Rev. Microbiol.* 9, 344–355.
- Shen, Y., and Bax, A. (2013). Protein backbone and sidechain torsion angles predicted from NMR chemical shifts using artificial neural networks. *J. Biomol. NMR* 56, 227–241.
- Souza, D.P., Andrade, M.O., Alvarez-Martinez, C.E., Arantes, G.M., Farah, C.S., and Salinas, R.K. (2011). A component of the Xanthomonadaceae type IV secretion system combines a VirB7 motif with a N0 domain found in outer membrane transport proteins. *PLoS Pathog.* 7, e1002031.
- Souza, D.P., Oka, G.U., Alvarez-Martinez, C.E., Bisson-Filho, A.W., Dunger, G., Hobeika, L., Cavalcante, N.S., Alegria, M.C., Barbosa, L.R.S., Salinas, R.K., et al. (2015). Bacterial killing via a type IV secretion system. *Nat. Commun.* 6, 6453.
- Trocter, M., Felisberto-Rodrigues, C., Christie, P.J., and Waksman, G. (2014). Recent advances in the structural and molecular biology of type IV secretion systems. *Curr. Opin. Struct. Biol.* 27C, 16–23.
- Vranken, W.F., Boucher, W., Stevens, T.J., Fogh, R.H., Pajon, A., Llinas, M., Ulrich, E.L., Markley, J.L., Ionides, J., and Laue, E.D. (2005). The CCPN data model for NMR spectroscopy: development of a software pipeline. *Proteins* 59, 687–696.
- Zamboni, D.S., McGrath, S., Rabinovitch, M., and Roy, C.R. (2003). *Coxiella burnetii* express type IV secretion system proteins that function similarly to components of the *Legionella pneumophila* Dot/Icm system. *Mol. Microbiol.* 49, 965–976.
- Zechner, E.L., Lang, S., and Schildbach, J.F. (2012). Assembly and mechanisms of bacterial type IV secretion machines. *Philos. Trans. R. Soc. B Biol. Sci.* 367, 1073–1087.